



Molecular catalysis science: Nanoparticle synthesis and instrument development for studies under reaction conditions



Elad Gross¹, Gabor A. Somorjai*

Lawrence Berkeley National Laboratory, 1 Cyclotron Rd., Berkeley, CA, United States
Department of Chemistry, University of California, Berkeley, CA, United States

ARTICLE INFO

Article history:

Received 9 July 2014

Revised 19 December 2014

Accepted 29 December 2014

Keywords:

Heterogeneous catalysis

In situ spectroscopy

SFG vibrational spectroscopy

X-ray spectroscopy

IR spectroscopy

ABSTRACT

The synthesis of architecturally designed catalytic nanostructures and their *in situ* characterization under reaction conditions enable the development of catalysts with improved stability, reactivity, and product selectivity. Throughout this review paper, we will explore three recent reports that demonstrate the invaluable synergetic impact of combining synthesis, catalysis, and *in situ* spectroscopy for catalysts development. In the first example, product selectivity in 1,3 butadiene hydrogenation reaction was tuned by employing size-selected Pt nanoparticles as catalysts. SFG vibrational spectroscopy measurements uncovered the mechanism that induced the size-dependent selectivity. The important role of metal/metal-oxide interface during CO oxidation reaction is demonstrated in the second part of this review paper. *In situ* synchrotron-sourced X-ray spectroscopy correlated between the oxidation state of the metal-oxide support and its impact on the catalytic reactivity of supported Pt nanoparticles. In the third example, dendrimer-encapsulated Au nanoparticles were used as catalyst for cascade reactions, which were previously catalyzed by homogeneous catalysts. Reactants into product evolution and the oxidation state of catalytically active Au nanoparticles within the flow reactor were mapped with micrometer-sized IR and X-ray beams. These three examples demonstrate the important role of colloidal synthesis and *in situ* spectroscopy measurements for in-depth analysis of structure–reactivity correlations.

© 2015 Elsevier Inc. All rights reserved.

1. Introduction

This review paper is dedicated to the memory of Haldor Topsoe, a giant in the field of catalysis. His understanding of the importance of the science as well as the technology development of catalytic processes set the example for others. His remarkable insight put his stamp on the field during past decades up to the present.

During the last few decades, there have been tremendous developments in catalysis research that shifted the research focus from studying simplified model-system into analysis of more realistic catalysts under reaction conditions. The main developments that initiated this progress were: (i) well-controlled synthesis of catalytic nanostructures [1–5] and (ii) advanced instrumentation for *in situ* characterization of catalytic processes under reaction conditions [6–12].

1.1. Development of model catalytic nanostructures

The development of well-controlled, simplified, catalytically active nanostructures which mimic the properties of industrial catalysts was conducted in two different routes. In the first approach, metallic nanoparticles were deposited within a UHV (Ultra-High Vacuum) environment on a single crystal which was coated with a thin layer of metal-oxide [5,13–15]. The UHV conditions enabled the preparation of well-defined oxide surfaces and size-controlled nanoparticles within a clean environment. Following this approach, different studies have demonstrated the impact of nanoparticle's size and shape [5,13,16–18] on the catalytic properties of the nanoparticles. Other UHV studies emphasized the impact of metal/metal-oxide interface and suggested that this interaction is the main reason for the enhanced reactivity [19,20,24].

One of the well-studied examples in this field was the size-dependent reactivity of oxide-supported Au nanoparticles toward CO oxidation reaction [17,18]. A variety of spectroscopic measurements were conducted to uncover the reasons for this unique reactivity [5,21–23]. For example, it was demonstrated that CO oxidation rate can be enhanced by up to three orders of magnitude following the deposition of 1–3 nm Au nanoparticles on MgO

* Corresponding author at: Department of Chemistry, University of California, Berkeley, CA, United States.

E-mail address: somorjai@berkeley.edu (G.A. Somorjai).

¹ Current address: Institute of Chemistry, The Hebrew University of Jerusalem, Israel.

surfaces [42,43]. DFT calculations indicated that while supporting Au₈ clusters on defect-rich MgO, an electronic charge is transferred from the metal-oxide support to the clusters. The combination of electron-rich Au clusters and high density of oxygen vacancies on the MgO surface facilitates O₂ dissociation at the Au–MgO interface and enhances the CO oxidation rate [15,18].

A different approach utilized the knowledge and capabilities of colloidal synthesis for the preparation of size- and shape-controlled catalytically active nanoparticles [1,3,25–28]. During the colloidal synthesis, different ligands stabilize the nanoparticles and direct their morphological properties. In this approach, the adsorption of ligands on the metal surface provides high control over the cluster properties but also lowers the number of accessible catalytic sites. Different methods were used in order to remove the ligands and minimize their impact on the catalytic reactivity [29–31]. It was recently demonstrated that by using oxygen plasma treatment, most of the surface-adsorbed ligands can be removed without changing the structure of the catalytically active nanoclusters [32]. For example, size-controlled Pt nanoparticles were deposited on TiO₂ surface and tested as catalyst in furfural hydrogenation reaction. In order to increase the metal–support interactions, the organic ligands were removed by oxygen plasma treatment. It was obtained that following this treatment, the formation rate of furfuryl alcohol was enhanced by 50-fold, when compared to SiO₂ supported nanoparticles, in which the support is catalytically inert. SFG (sum frequency generation) vibrational spectroscopy measurements indicated that reactants adsorption on the TiO₂ surface modified the product selectivity due to strong interaction between the oxide surface and the furfural's carbonyl group [32].

1.2. Advanced instrumentation for *in situ* characterization of catalytic processes

Development of spectroscopic tools which are capable of *in situ* characterization of catalytic processes enables to analyze the properties of catalysts under reaction conditions. High-pressure STM (scanning transmission microscope) was applied to study the structural changes in catalytic surfaces [33,34]. A variety of vibrational spectroscopy methods were utilized to follow the reactant to product transformation [35,36]. Among these methods are surface sensitive techniques such as SFG (sum frequency generation) vibrational spectroscopy [32,37] and PM-IRAS (polarization modulation infrared reflection absorption spectroscopy) [38,39] that detect active intermediates during catalytic reactions. Time resolved IR spectroscopy measurements analyze the kinetic properties of catalytic reactions [40,41] while IR microspectroscopy can track the spatial distribution of reactants and products within the catalyst [42–44].

The expansion of synchrotron-based X-ray spectroscopy techniques provides effective tools to study the dynamic electronic properties of catalysts under reaction conditions. HP-XPS (high-pressure X-ray spectroscopy), EXAFS (extended X-ray absorption fine structure) and NEXAFS (near edge X-ray absorption fine structures) spectroscopy measurements detect the oxidation state, coordination number, and composition of catalysts [45,46]. High spatial resolution XRD (X-ray diffraction) and EXAFS microspectroscopy along with X-ray tomography measurements tracked the dynamic changes in the structure and composition of catalysts [47–50]. These *in situ* measurements demonstrated that the catalytic surface is dynamic and its structure, composition, and electronic properties can be widely modified under reaction conditions. The dynamic nature of catalysts further emphasizes the importance of *in situ* spectroscopy measurements for in-depth analysis of catalytic processes.

In this review, we will focus on three case studies that demonstrate the powerful capabilities gained by combining synthesis of well-defined nanostructures, their application as catalysts and *in situ* spectroscopy of the catalytic reaction. These examples show that *in situ* spectroscopy measurements are crucial for the analysis of catalytic processes and for optimization of catalysts (Fig. 1).

In the first example, the structure–reactivity correlations of catalytically active Pt nanoparticles toward hydrogenation of 1,3 butadiene were studied. Different reaction intermediates were detected by *in situ* SFG vibrational spectroscopy by changing the nanoparticles size [51]. In the second example, a variety of mesoporous metal-oxide supports were prepared and tested as catalysts for CO oxidation reaction, with and without the addition of Pt nanoparticles [52]. The correlation between the reaction rates and oxidation state of the metal-oxide support was analyzed with *in situ* synchrotron-based NEXAFS and HP-XPS. In the third example, highly oxidized Au nanoparticles were packed in flow reactor and used as catalyst toward cascade reactions that were previously activated by homogenous catalysts [42]. The combination of *in situ* IR and X-ray microspectroscopy tracked the reactant into product evolution and the oxidation state of the catalyst within the flow microreactor. These measurements correlated between the oxidation state of the catalyst along the flow reactor and its catalytic reactivity and selectivity.

2. Molecular catalysis science: the combination of synthesis, spectroscopy, and catalytic reactivity

2.1. The impact of the size of Pt nanoparticles on the product selectivity in hydrogenation of 1,3 butadiene

In many catalytic processes, the product distribution can be modified by changing the size of catalytically active metallic nanoparticles [53,54]. The size-dependent selectivity is obtained due to changes in the geometric and electronic properties of the nanoparticle as its size is decreased below 10 nm [55]. Geometric effects include the size dependence distribution of kinks, steps, and terrace sites which are exposed on the metal surface and are highly active during the catalytic process. Electronic effects indicate the changes in the location of the d-band center, which is correlated to the interaction between the metal surface and adsorbate molecules [56]. Different studies have demonstrated that product distribution can be tuned by modifying the cluster size in the range of 1–10 nm. In this size regime, small changes in the cluster size would have an immediate impact on both its electronic and geometric properties [57,58].

In this study, polyhedral Pt nanoparticles in the size range of 1–7 nm were synthesized using polyol methods and capped with PolyVinylPyrrolidone (PVP) ligands to prevent cluster aggregation. Pt clusters with different sizes were synthesized by changing the reaction temperature and the amount of PVP and Pt precursor.

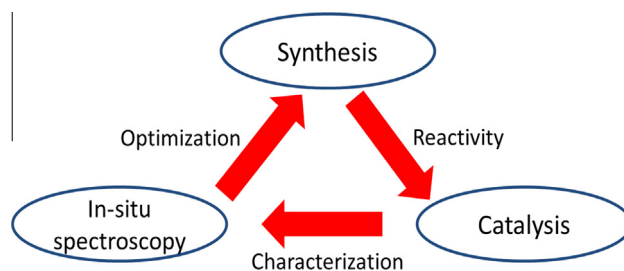


Fig. 1. Combining synthesis of nanoparticles, reactivity measurements, and *in situ* spectroscopy for characterization and optimization of the catalytic properties of catalysts.

The colloidal synthesis enabled the formation of Pt nanoclusters with narrow size distribution of up to $\pm 25\%$ (Fig. 2). The different clusters were then tested as catalysts toward the hydrogenation reaction of 1,3 butadiene (1,3-BD) (Fig. 3a).

Partial hydrogenation of 1,3-BD can lead to the formation of three isomers: *cis* 2-butene, *trans* 2-butene, and 1-butene. Saturated *n*-butane product can be formed as well by the complete hydrogenation of the reactant. The product distribution as function of Pt nanoparticles size is demonstrated in Fig. 3b. The catalytic measurements were performed at 75 °C with 10 torr of 1,3-BD, 100 torr of H₂, and 650 torr of balancing He. The selectivity was calculated according to the products formation at conversion rate of less than 10%.

The product distributions show high dependence in cluster size, indicating that this catalytic reaction is indeed structure sensitive. Increased selectivity toward full hydrogenation products was detected as the particle size decreased. For cluster size above 4 nm, the main products were butene isomers. Similar product distribution was measured with Pt(111) and Pt(100) single crystals which showed up to 90% selectivity toward the unsaturated butene isomers products [59]. By decreasing the Pt nanoparticles size below 2 nm, the ratio between partial to full hydrogenation products was modified to 2:3. These results indicate that product selectivity can be tuned by up to 6-fold simply by changing the nanoparticle size. The similarity in product selectivity of large Pt nanoparticles and Pt single crystals indicates that at this size regime, the catalytic properties of the nanoparticles are similar to that of bulk Pt.

The size-dependent selectivity specifies that there are inherent differences in the reaction pathways for 1,3-BD hydrogenation on Pt nanoparticles with various sizes. To elucidate the observed selectivity differences, *in situ* SFG vibrational spectroscopy was employed under reaction conditions to monitor the reaction intermediates as function of cluster size (Fig. 4).

SFG vibrational spectroscopy is a surface sensitive technique that exclusively probes molecules at the interface. The analysis of molecules that reside at the solid–gas interface provides a unique capability to probe the most stable long-lived intermediates. The SFG signal was formed by spatially and temporally overlapping a visible beam (532 nm) and a tunable IR (2680–3180 cm⁻¹) beam at the surface of silica prism (Fig. 4b). Pt nanoparticles were deposited on the surface of the prism which capped the reaction cell. The SFG signal was induced from the *z*-component of adsorbate molecules, which reside at the solid–gas interface, sensitive both to the concentration and orientation of the interfacial species.

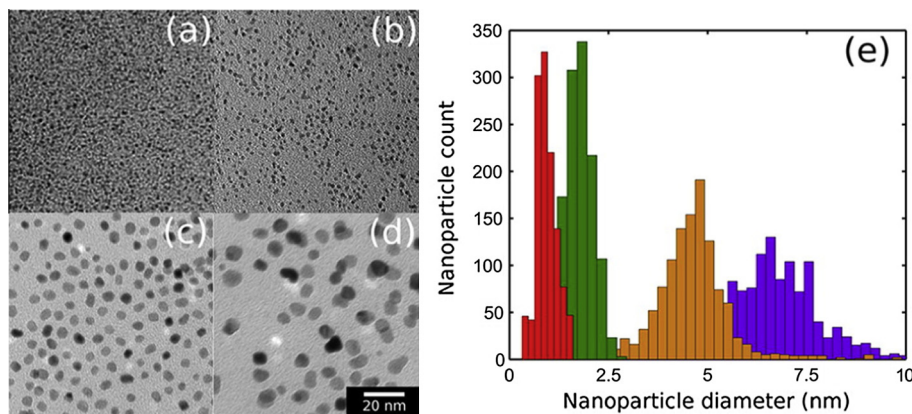


Fig. 2. Transmission electron microscopy images of polyhedral Pt nanoparticles. Panels (a), (b), (c), and (d) show nanoparticles with an average diameter and standard deviation of 0.94 ± 0.26 , 1.80 ± 0.34 , 4.63 ± 1.12 , and 6.67 ± 1.20 nm, respectively. Panel e shows particle-size distributions for the four particle sizes. The 20 nm scale bar in panel d reflects the scale for all images.

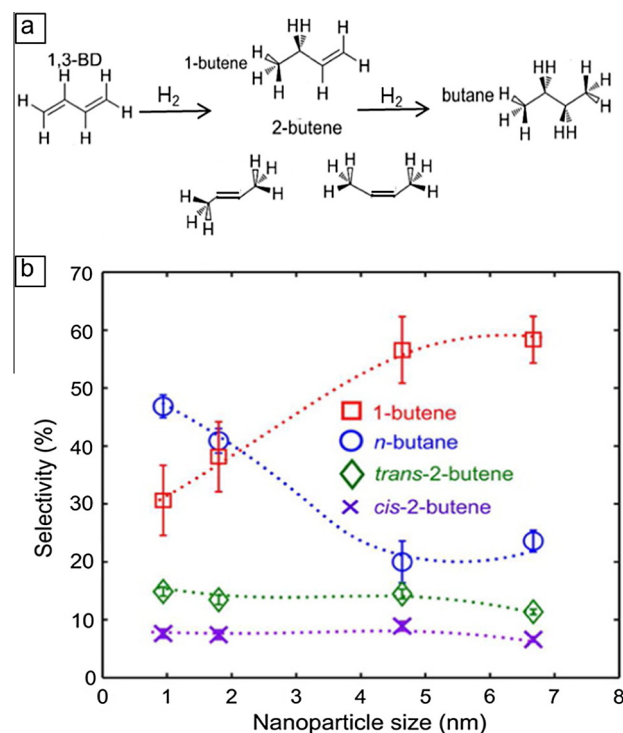


Fig. 3. (a) Reaction scheme 1,3 BD hydrogenation. (b) Product selectivity for 1-butene (\square), *n*-butane (\circ), *trans*-2-butene (\diamond), and *cis*-2-butene (\times) from the conversion of 1,3 butadiene (1,3-BD) hydrogenation ($T = 75$ °C with 10 Torr of 1,3-BD, 100 Torr of H₂, and 650 Torr of He) as a function of nanoparticle size.

The vibrational spectra that were detected during 1,3-BD hydrogenation reaction are shown in Fig. 4a. Blue circles and dashed red lines indicate the average and standard deviation over nine SFG spectra, respectively, while the solid black line represents the best-fit model spectra. The SFG spectra were correlated to the catalytic selectivity and indicated that the intermediates formed with small (0.9 and 1.8 nm) nanoparticles are different than that of the large (4.6 and 6.7 nm) nanoparticles.

The SFG spectra of the larger nanoparticles exhibit a dominant peak at ~ 2878 cm⁻¹, which was assigned to the symmetric stretch of CH_{3(s)}. In addition, a shoulder peak was located at 2906 and 2979 cm⁻¹, which corresponds to methylene stretch (CH_{2(FR)}) and the asymmetric stretch of CH₃ (CH_{3(a)}), respectively. Four bands

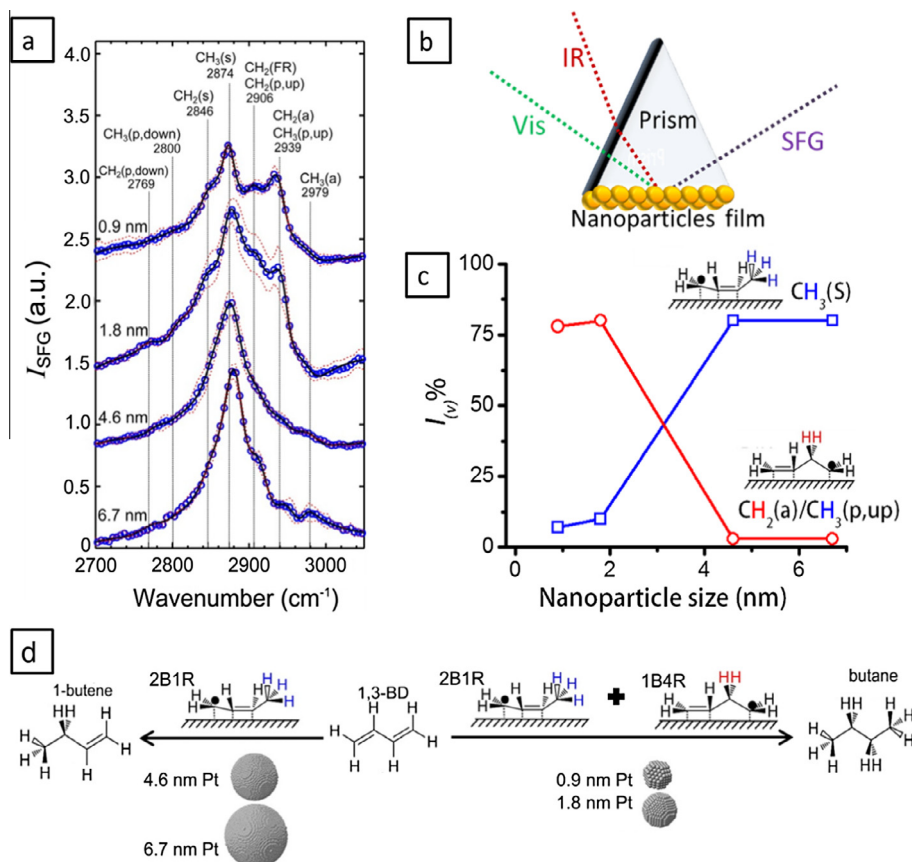


Fig. 4. (a) *In situ* SFG vibrational spectra of reaction intermediates produced on Pt nanoparticles during 1,3-BD hydrogenation. Blue dots and red dashed lines represent averages and standard deviations of nine SFG spectra, respectively. Assignments of vibrational bands are based on model spectra. (b) The SFG signal was generated from visible beam and tunable IR beam which were spatially and temporally overlapping at the surface of a Silica prism on which a layer of Pt nanoparticles was deposited. (c) Normalized SFG intensity for $\text{CH}_2(\text{a})/\text{CH}_3(\text{p,up})$ (\circ) and $\text{CH}_3(\text{s})$ (\square) vibrational modes as a function of nanoparticle size. Small nanoparticles have an increased contribution to the SFG signal from the $\text{CH}_2(\text{a})/\text{CH}_3(\text{p,up})$ modes, whereas large particles are dominated by the $\text{CH}_3(\text{s})$ mode. The methylene and methyl groups that exhibit SFG signal are highlighted in red and blue, respectively. (d) The impact of nanoparticles' size on the formation of different intermediates and the induced products selectivity. (For interpretation of the references to colour in this figure legend, the reader is referred to the web version of this article.)

construct the primary SFG spectral features of the small nanoparticles. The four peaks (2846 , 2874 , 2906 , and 2939 cm^{-1}) were assigned to the symmetric stretch of CH_2 ($\text{CH}_2(\text{s})$) and CH_3 ($\text{CH}_3(\text{s})$), the fundamental methylene stretching mode ($\text{CH}_2(\text{FR})$), and methylene asymmetric stretch ($\text{CH}_2(\text{a})$).

In order to better illustrate the catalytic and spectroscopic correlations, normalized SFG intensities of the $\text{CH}_2(\text{a})/\text{CH}_3(\text{p,up})$ and $\text{CH}_3(\text{s})$ as function of the nanoparticles size were plotted (Fig. 4c). The increase in $\text{CH}_2(\text{a})/\text{CH}_3(\text{p,up})$ ratio with small nanoparticles provides an indication for the accessible route leading to the formation of saturated butane product. SFG signals indicate the development of both 1-buten-4-yl and 2-buten-1-yl radicals on small nanoparticles, which provide favorable pathways for *n*-butane formation.

It was previously demonstrated that small nanoparticles exhibit an increase in the density of step and corner sites at the expense of terrace sites [55,56]. The high density of atoms with lower coordination number will shift the d-band center location and increase the number of empty anti-bonding states. As a consequence, reactant–metal interactions will increase. Moreover, a higher d-band center makes the surface more reactive by lowering the transition state energy of reactant molecules, uncovering additional pathways toward product formation [15,18].

High density of low-coordination sites on small nanoparticles will also modify the binding geometry of reactants and intermediates on the metal surface. These changes in the surface structure will give rise to the formation of different intermediates which could not be obtained on bigger nanoparticles or on terrace sites.

The *in situ* SFG vibrational spectroscopy measurements indicated that 0.9 and 1.8 nm Pt nanoparticles provide modified adsorption sites (e.g., low-coordination sites) that facilitated H-insertion both to the internal carbon and terminal carbon. The 4.6 and 6.7 nm Pt nanoparticles favor H-insertion at the terminal carbon, as also observed on Pt bulk materials (Fig. 4d). These results suggest that the presence of low-coordination sites promotes H-insertion at the internal carbon (in addition to the external carbon), which are not obtained in bigger nanoparticles, either due to electronic or due to geometric effects.

2.2. Enhanced CO oxidation rate at the interface of mesoporous oxide and Pt nanoparticles

It was widely demonstrated that the catalytic reactivity of metallic nanoparticles can be enhanced following their deposition on designated metal-oxide supports [19,20,32]. Different studies have indicated that the development of strong metal–support interactions (SMSI) increases the catalytic reactivity by either tuning the electronic properties of the metal [27,60] or due to the formation of a highly active metal/metal-oxide interface [21]. The exact mechanism that governs these catalytic reactions was not fully understood, due to limited insight of the metal/metal-oxide interface during the catalytic reaction. Synchrotron-based measurements make it possible to study the structure and composition of complex catalytic systems under reaction conditions.

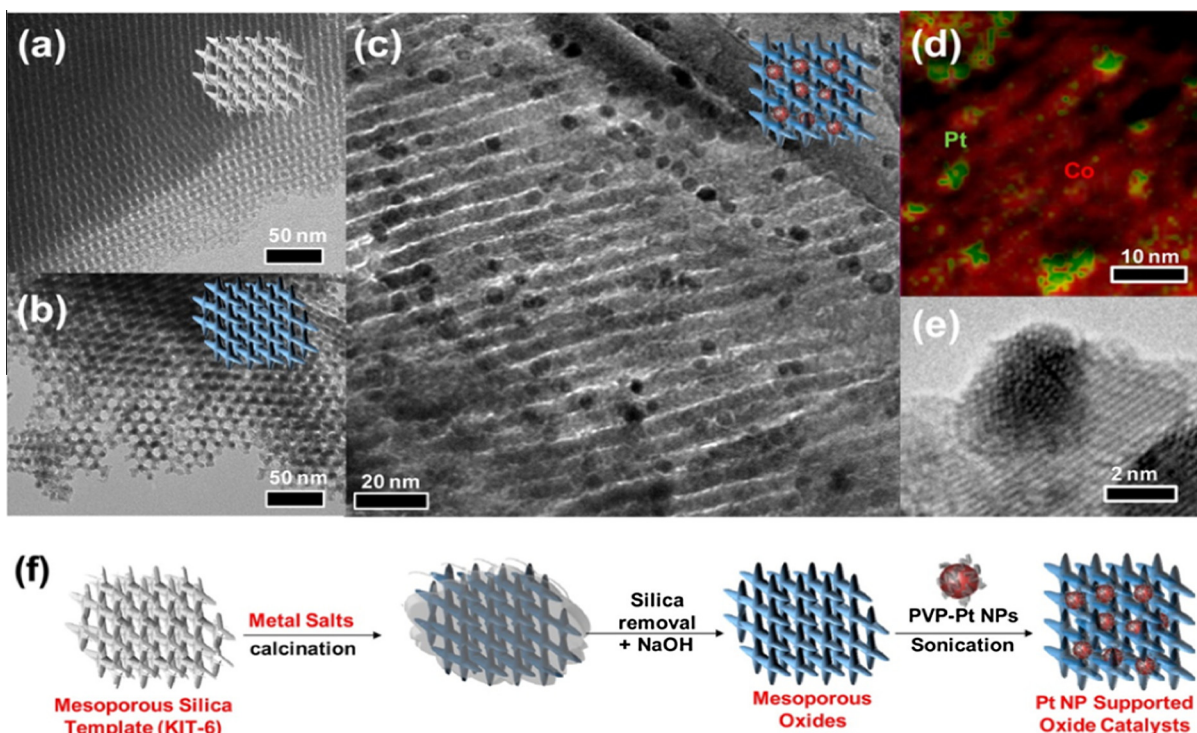


Fig. 5. Preparation of Pt-nanoparticle-loaded Co_3O_4 catalysts. TEM images of (a) mesoporous silica template and (b) the resulting Co_3O_4 replica. TEM image of (c) Pt/ Co_3O_4 catalysts and (d) their corresponding energy-dispersive spectroscopy (EDS) phase mapping, showing the distribution of Co (red) and Pt (green) atoms on the surface. (e) High-resolution TEM image of Pt/ Co_3O_4 catalysts. (f) Illustration of the hard-templating approach for the preparation of mesoporous-oxide-supported Pt nanoparticle catalysts.

A variety of mesoporous oxides (Co_3O_4 , NiO , MnO_2 , Fe_2O_3 , and CeO_2) were synthesized and loaded with size-controlled Pt nanoparticles to investigate the metal/metal-oxide interface effect on CO oxidation reaction rate. The mesoporous oxides were prepared through hard template approach [61]. In this method, mesoporous silica was used as a template on which a specific metal-oxide was impregnated. The mesoporous silica was then removed by base, forming the pure mesoporous metal-oxide replica (Fig. 5). Following the formation of crystalline metal-oxide, PVP-capped Pt nanoparticles with an average diameter of 2.5 nm were incorporated within the channels of the mesoporous oxide.

The pure mesoporous oxide supports showed notable catalytic reactivity in the absence of a metal, for example, TOF rates of 0.015 and 0.01 s^{-1} were measured with Co_3O_4 and NiO , respectively (under reducing conditions of 100 Torr CO, 40 Torr O_2 , and 473 K). The incorporation of Pt nanoparticles within the mesoporous oxides increased the catalytic reactivity by more than two orders of magnitudes (Fig. 6).

The measured CO oxidation rates for Pt/ Co_3O_4 and Pt/ NiO were 500 and 1.1 s^{-1} , respectively. It should be noted that the TOF rate of SiO_2 supported Pt nanoparticles, in which the support is catalytically inert, was 0.1 s^{-1} . The reactivity of oxide-supported metallic catalysts was significantly higher than the combined reactivity of the metal-oxide itself and the Pt nanoparticles. For example, the combined reactivity of silica-supported Pt nanoparticles and Co_3O_4 (without Pt) was 0.11 s^{-1} , while the reaction rate of Pt/ Co_3O_4 was 500 s^{-1} . This result indicates an enhancement of 3 orders of magnitude in the reaction rate due to the formation of metal/metal-oxide interface. The enhanced reactivity can be explained in the following mechanism: CO is adsorbed on the Pt surface and diffuses to the metal/metal-oxide interface (Fig. 6b, inset). CO will then interact with active oxygen in the lattice of the metal-oxide support. The last step will be the refill of oxygen vacancies in the oxide by gaseous O_2 [15,18].

In order to understand the reasons for enhanced reactivity of oxide-supported Pt nanoparticles, *in situ* NEXAFS and XPS measurements were conducted under reaction conditions (Fig. 7). The different supported catalysts were exposed to CO and O_2 mixture at 473 K. The NEXAFS total electron yield (TEY) spectra of the metal L edge were monitored by detecting the compensating electrons from ground to sample.

The Co L edge of Pt/ Co_3O_4 was monitored under reducing (39 torr CO and 15 torr O_2) and oxidizing (15 torr CO and 39 torr O_2) conditions at 473 and 523 K. NEXAFS measurements revealed that the metal-oxide support is transformed from Co_3O_4 into CoO under reducing conditions at 523 K. The lower oxidation state of the support induced stronger interaction with O_2 molecules, facilitating their dissociation and enhancing the CO_2 formation rate. These results demonstrate the important role of the oxidation state of the metal-oxide during catalytic reaction.

The reaction rate over oxide-supported Pt nanoparticles can be enhanced by tuning the redox properties of the metal-oxide. Even after O_2 -deficient conditions, active oxygen was provided from the lattice of the oxide to facilitate the catalytic reaction. The redox properties of the metal-oxide support provide the activated oxygen at the metal/metal-oxide interface, which enhances the catalytic rate. As analyzed by *in situ* X-ray measurements, the correlation between surface redox chemistry and catalytic reactivity offers a unique way to tune the catalytic reactivity by controlling the electronic properties of the metal-oxide support.

2.3. Bridging the gap between homogeneous and heterogeneous catalysis with dendrimer-encapsulated Au nanoparticles

Continuous efforts in catalysis research have been devoted to the activation of heterogeneous catalysts toward reactions that are mainly activated by homogeneous catalysts [62]. Replacing homogeneous catalysts with heterogeneous catalysts enhances

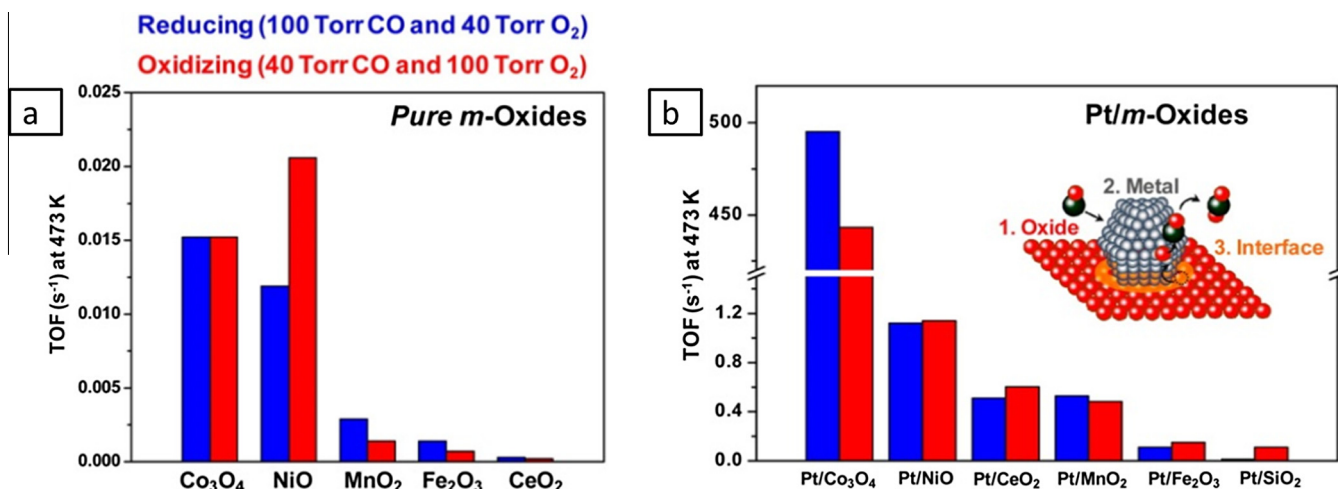


Fig. 6. CO oxidation over (a) pure mesoporous oxides and (b) Pt-nanoparticle loaded on oxide catalysts. The inset in (b) is an illustration showing the potential reaction sites of Pt nanoparticles loaded on metal oxide during CO oxidation.

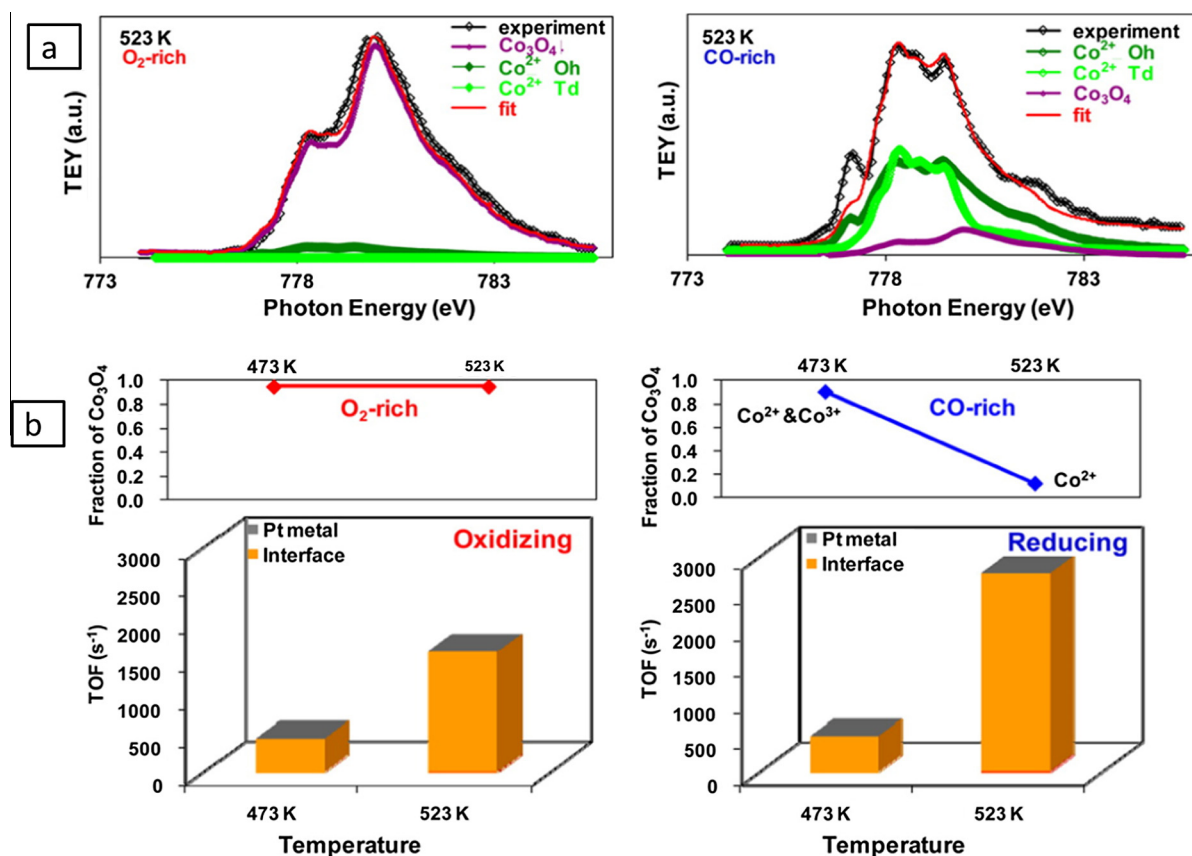


Fig. 7. (a) NEXAFS TEY spectra at the Co L edges for the Pt/Co₃O₄ catalyst and (b) graphs correlating the catalytic activity (TOF) and oxidation state of Co in CO oxidation. Shown in (a) are representative linear-combination fittings obtained at 523 K under (left) 15 Torr CO and 39 Torr O₂ (O₂-rich) and (right) 39 Torr CO and 15 Torr O₂ (CO-rich) conditions. The bar graphs showing the total TOFs of the Pt/Co₃O₄ catalyst have been decomposed into the contributions of pure Pt (in gray) and the Pt–Co₃O₄ interface (in orange). (For the interpretation of the references to color in this figure legend, the reader is referred to the Web version of this article.)

the sustainability of the catalytic reaction, providing a highly recyclable, scalable and efficient setup. It was recently reported that small (<2 nm) metallic nanoclusters, encapsulated in a dendrimer matrix and supported on mesoporous SiO₂, show unique reactivity and selectivity toward a wide array of π -bond activation reactions that are mainly catalyzed by homogeneous catalysts [58,63–66]. The small size of the nanoparticles enables reversible oxidation

of the metal clusters into catalytically active metal ions [66,67]. Encapsulation of the metal within the dendrimer matrix prevents the leaching of highly oxidized metal ions into the solution phase, inducing high catalytic stability and recyclability of the catalyst. Activation of complex organic reactions with heterogeneous catalysts provides unique opportunities to control and direct the product selectivity. For example, by tuning the packing density of the

polymeric matrix that encapsulates the metal cluster and maximizing its steric effect, the product diastereoselectivity can be modified [63,64]. In addition, as will be further demonstrated in the following paragraphs, the product selectivity in multistep reactions can be tuned by changing the residence time of reactant molecules within a flow reactor [42,64].

Dendrimer-encapsulated Au nanoparticles with diameter of 2 nm were loaded on mesoporous SiO₂, packed in a flow microreactor, and utilized as a heterogeneous catalyst for the cascade reaction of dihydropyran synthesis (Fig. 8a). In this reaction, propargyl vinyl ether **1** was catalytically rearranged by the Au catalyst into the primary product, allenic aldehyde **2**. Activation of the primary product **2** by the Au catalyst was followed by nucleophilic attack of butanol-d₁₀, leading to the formation of the secondary product, acetal **3**. In order to track the catalytic transformation within the flow microreactor, this multistep reaction was mapped with a spatial resolution of 15 μm, employing synchrotron-sourced IR and X-ray beams. High-resolution mapping of the catalytic reaction with IR microspectroscopy detected the reactant into product evolution, while X-ray microspectroscopy revealed the oxidation state of the catalyst along the flow reactors (Fig. 8b).

Prior to the catalytic reaction, dendrimer-encapsulated Au nanoparticles were oxidized to Au ions by a flow of an inorganic oxidizer, PhCl₂, solvated in toluene. Following the formation of catalytically active, highly oxidized Au ions, the catalyst was tested toward the cascade reaction of dihydropyran formation.

The product selectivity was tuned by modifying the residence time of the reactants. High flow rate of 10 mL/h induced low conversion (20%) and a primary:secondary (**2**:**3**) product ratio of 5:1. Higher yield (75%) was obtained by decreasing the flow rate by 50-fold to 0.2 mL/h, while the product selectivity (**2**:**3**) was transformed to 0:100 (Fig. 8b). These results demonstrate the advantage in performing catalytic transformations in flow microreactors, enabling isolation of either the primary or the secondary products [42,60,64]. Tunable selectivity between different products in cascade reactions is not easily achieved while employing homogeneous or heterogeneous catalysts in a batch reactor. Though isolation of

the secondary product is possible in batch mode reactions, the exclusive formation of primary product is not a simple task.

In the cascade dihydropyran formation reaction, each of the reactants and products shows distinguishable IR signatures (Fig. 9a and b). As a consequence, the transformation of reactants into products can be visualized with IR microspectroscopy. The IR measurements were performed along the flow reactor with continuous reactant flow, ensuring that the reactant and product concentrations at each point along the flow reactor were at steady state (Fig. 9c).

With a flow rate to 1 mL/h (Fig. 9a), a decrease in the reactant, vinyl ether **1**, absorption peaks amplitude (around 1150–1250 cm⁻¹) was indicated and followed by the formation of a strong absorption peak of the primary product, aldehyde **2**. After 0.2 mm, a gradual decrease in the aldehyde absorption peak along with a comparable decrease in the higher energy (between 2300 and 2700 cm⁻¹) absorption spectra regime indicated the parallel consumption of butanol-d₁₀ and aldehyde **2** to the formation of the secondary product, acetal **3**.

Higher reaction rates were obtained when increasing the residence time of the reactants by 5-fold (Fig. 9b), as obtained by the complete loss of the reactant's absorption peaks at 1150–1250 cm⁻¹ after 0.6 mm. Though primary product, **2**, was initially formed, after 0.4 mm, the aldehyde IR signature was fully lost. This result indicates the catalytic transformation from primary into secondary product. The formation of secondary product, acetal **3**, is demonstrated as well by the total consumption of butanol-d₁₀, as observed by the gradual decrease of the O–D absorption peak at 2300–2650 cm⁻¹ until its disappearance after 0.8 mm. At this flow rate, consumption of the reactant was followed by the formation of the primary product, which then further transforms into the secondary product.

Subsequent to the FTIR microspectroscopy measurements, the reactants and products were also analyzed by GC. All the conclusions, both regarding the catalytic reactivity and product selectivity, which were derived from the IR measurements, were supported by the GC analysis. The synchrotron-based IR microreac-

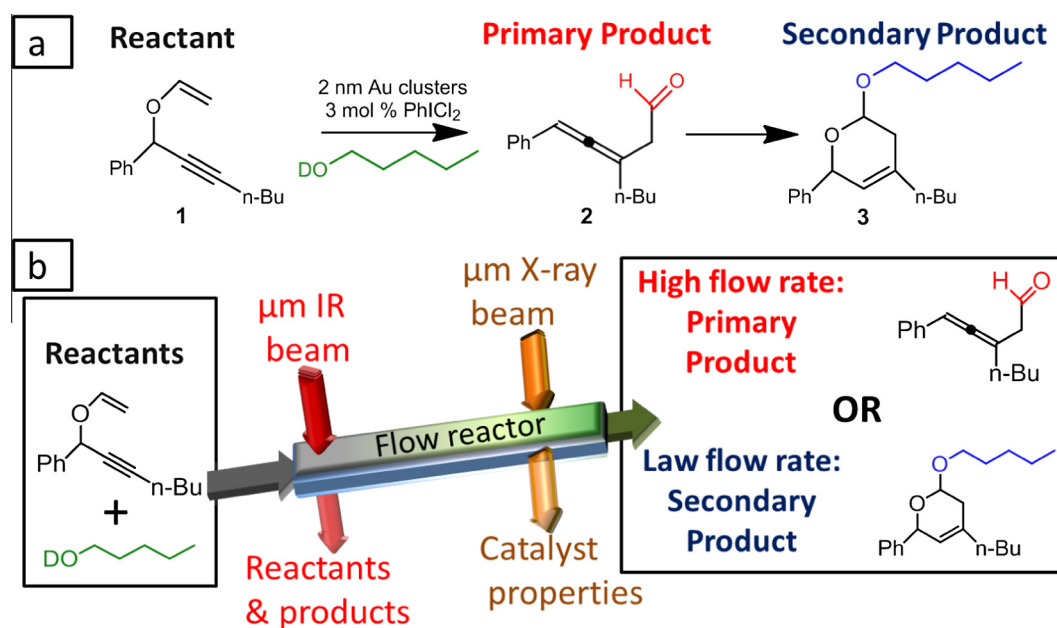


Fig. 8. (a) Scheme of the cascade reaction. (b) Product selectivity toward primary or secondary products was determined according to the flow rate of reactants through the flow reactor. μm sized IR beam tracked the reactants into product evolution within the flow reactor, while μm X-ray beam followed the oxidation state of the catalyst under reaction conditions.

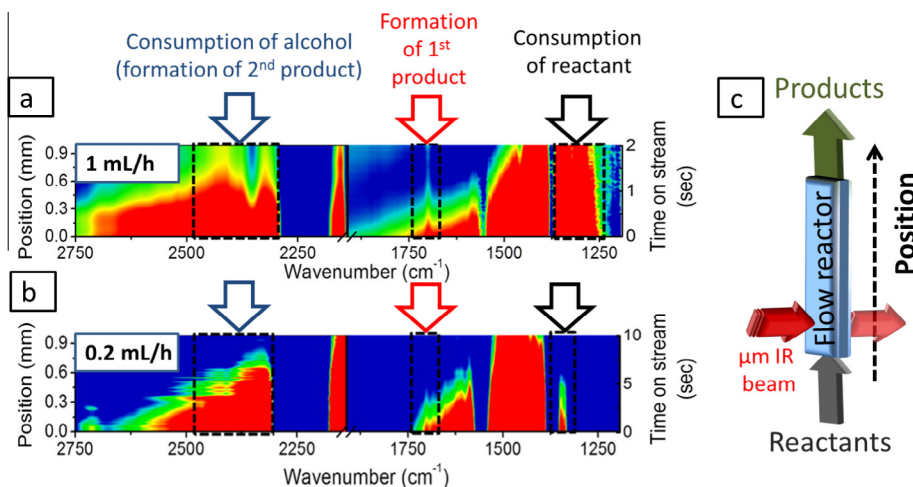


Fig. 9. IR absorption microspectroscopy scans along the flow reactor with reactants flow rates of 1 (a) and 0.2 (b) mL/h. Markers were added to direct the eye toward the changes in the IR spectra at different flow rates. A scheme of the micro-IR flow reactor is shown in (c).

tor and the lab-based stainless-steel microreactor were designed to have similar inner volume, ensuring comparable residence time of the reactants. GC analysis verified that the yield and selectivity of the products in these two microreactors were comparable, with variations of up to $\pm 15\%$.

A detailed kinetic analysis of the catalytic reaction was performed by integrating the IR absorption peaks of the reactants and products along the flow reactor (Fig. 10). The evolution of the reaction at flow rate of 1 mL/h can be divided into two parts (Fig. 10a). In the first part of the reaction (0–0.3 mm), vinyl ether **1** was consumed for the formation of allenic aldehyde **2**. During the second part of the reaction, the secondary product was formed and a linear decrease (zero order kinetics) in the concentration of the two reactants was measured.

The kinetic evolution of the reaction at slower flow rate of 0.2 mL/h was divided into three phases (Fig. 10b). During the initial phase of the reaction (0–0.14 mm), the concentration of reactant **1** gradually decreased due to the formation of primary product **2**. Within this incubation time, no formation of secondary product **3** or consumption of butanol- d_{10} were detected. Through the second part of the reaction (0.14–0.52 mm), the two reactants (vinyl ether **1** and butanol- d_{10}) and the primary product (allenic aldehyde **2**) were consumed along with the formation of the secondary product, acetal **3**. At this stage of the reaction, the local concentrations of the two reactants (vinyl ether **1** and butanol- d_{10}) saturate the catalyst, inducing zero order kinetics. The similarities in the con-

sumption rate of the two reactants are consistent with the fast transformation of primary product **2** into secondary product **3**, indicating that the rate determining step is the conversion of reactant **1** into primary product **2**. At the third phase of the reaction (0.52–1 mm), the concentration of the reactants was low enough to change the reaction kinetics from zero to first order for the two reactants. At this step, a continuous low, steady state concentration of allenic aldehyde **2** was detected, demonstrating its essential role as an intermediate for the formation of the secondary product, acetal **3**.

NEXAFS microspectroscopy measurements along the flow reactor revealed that after 2 mm, the concentration of the catalytically active Au(III) species was gradually decreasing due to Au(III) reduction into Au(0). The reduction process was correlated to the nucleophilic properties of butanol- d_{10} , which reduce the Au(III) back to its metallic state.

Based upon the IR and X-ray measurements, the catalytic system was further optimized to enhance the reactivity and decrease the deactivation rate of the catalyst. The reactant concentration was decreased in order to lower the reduction rate of Au(III) by butanol- d_{10} . NEXAFS results indicated that only the initial part of the reactor was active during the catalytic process. According to this observation, the total amount of Au catalyst was reduced by an order of magnitude and the length of the microreactor was decreased from 2 cm to 2 mm. Though the amount of the catalyst was reduced by an order of magnitude, only negligible decrease

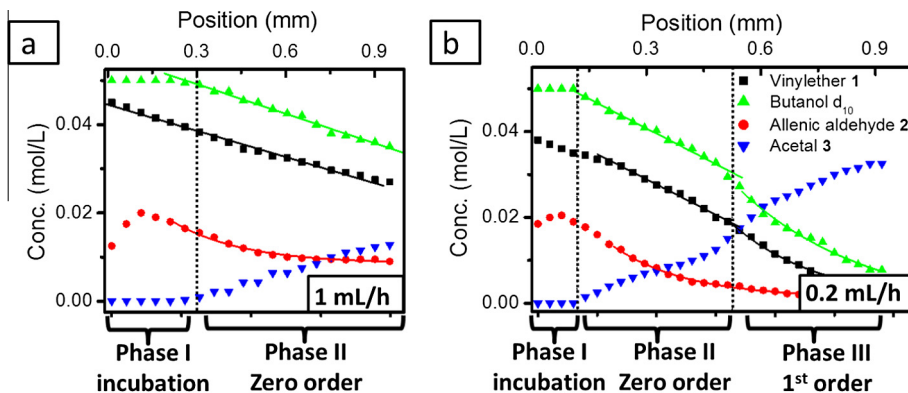


Fig. 10. Analysis of distribution of reactants and products as a function of location along the flow reactor at a flow rate of 1 (a) and 0.2 (b) mL/h. The absorption values of the reactants and products were integrated from the matching IR absorption peak areas and converted to concentration based on GC analysis of the solution. The dotted lines indicate the different stages of the catalytic reaction.

was obtained in the catalytic reactivity. These results indicate the importance of *in situ* spectroscopy of the catalytic reaction for analysis and optimization of catalytic processes.

3. Conclusions

The combination of (i) synthesis of catalytic nanostructures, (ii) testing their catalytic properties, and (iii) *in situ* spectroscopic analysis provides powerful capabilities to investigate and optimize catalytic processes. In this review paper, three recent examples from our research group demonstrated the advantages of this approach.

In the first example, it was shown that the mechanism for size-dependent catalytic selectivity can be revealed by *in situ* SFG vibrational spectroscopy. Gas-phase hydrogenation of 1,3-butadiene by size-selected Pt nanoparticles induces the production of either fully or partially saturated products. SFG analysis indicated the formation of different intermediates in accordance with the Pt cluster size, revealing the mechanism for size-dependent product selectivity. In the second example, synchrotron-based X-ray spectroscopy tracked the oxidation state of catalysts under reaction conditions. It was demonstrated that CO oxidation rate can be dramatically enhanced by loading catalytically active Pt nanoparticles on mesoporous metal-oxide. NEXAFS and HP-XPS spectroscopy analyzed the oxidation state of the metal-oxide surface under reaction conditions, correlating between oxidation state and the catalytic rate.

The combination of spectroscopy and microscopy measurements for high spatial resolution analysis of catalytic reactions was demonstrated in the third example. By combining X-ray and IR microspectroscopy analysis, the reactant to product evolution and the electronic properties of the catalyst within a flow reactor were detected. *In situ* synchrotron-sourced IR microspectroscopy detected the evolution of reactant into primary and then into secondary product. By tuning the residence time of the reactants in a flow microreactor, a detailed kinetic analysis of the reaction was performed. The utilization of different spectroscopic tools under reaction conditions gives access to invaluable data regarding the properties that govern the catalytic reaction. As demonstrated throughout this review paper, spectroscopic analysis can be utilized for preparation of better catalysts, with optimized stability, reactivity, and selectivity.

Looking ahead, the field of *in situ* spectroscopy of catalytic reactions can be further developed in two parallel routs:

- (I) Combining few spectroscopic tools that simultaneously analyze the catalytic reaction and enable a comprehensive analysis of catalytic processes [35,68,69]. For example, the hydrothermal crystallization process of zeolites from amorphous precursor gel into a crystalline microporous material was detected with combined *in situ* X-ray and Raman spectroscopy [70]. This study revealed fundamental insights regarding the construction of catalytic nanostructures, correlating between the vibrational spectrum, as revealed by Raman spectroscopy and the structural and electronic properties, as detected by X-ray spectroscopy.
- (II) Increasing the spatial resolution of microspectroscopy measurements into the nanoscale size regime [71–73]. A variety of studies indicated the capabilities of IR and X-ray spectroscopy at the nanoscale. In a recent example, X-ray measurements were conducted to visualize the microstructural evolution of lithium-ion batteries [47] and catalysts [74] under reaction conditions. *In situ* 3D quantitative analysis of structural changes at the nanoscale offers a direct way to understand the mechanical changes in catalytic nanostructures under reaction conditions. Another promising approach utilizes tip-enhanced IR and Raman spectroscopy

as a route to further enhance the spatial resolution of microspectroscopy measurements into the nanoscale [75–77]. These novel spectroscopic methods are expected to open up new levels of fundamental understanding of catalytic processes which cannot be otherwise accessed.

Acknowledgments

This work was supported by the Director, Office of Basic Energy Sciences, Materials Science and Engineering Division and the Division of Chemical Sciences, Geological and Biosciences of the U.S. Department of Energy under Contract No. DE-AC02-05CH11231. Work at the Molecular Foundry was supported by the Director, Office of Science, Office of Basic Energy Sciences, Division of Material Sciences and Engineering, of the U.S. Department of Energy under Contract No. DE-AC02-05CH11231. The X-ray absorption spectroscopy and IR microspectroscopy studies were performed at the Advanced Light Source, a DOE User facility of the Office of Science, Office of Basic Energy Sciences.

References

- [1] K. An, G.A. Somorjai, Size and shape control of metal nanoparticles for reaction selectivity in catalysis, *Chemcatchem* 4 (2012) 1512–1524.
- [2] K. Na, Q. Zhang, G.A. Somorjai, Colloidal metal nanocatalysts: synthesis, characterization, and catalytic applications, *J. Clust. Sci.* 25 (2014) 83–114.
- [3] H. Zhang, M.S. Jin, Y.J. Xiong, B. Lim, Y.N. Xia, Shape-controlled synthesis of Pd nanocrystals and their catalytic applications, *Accounts Chem. Res.* 46 (2013) 1783–1794.
- [4] B.R. Cuenya, Synthesis and catalytic properties of metal nanoparticles: size, shape, support, composition, and oxidation state effects, *Thin Solid Films* 518 (2010) 3127–3150.
- [5] M.S. Chen, D.W. Goodman, Structure-activity relationships in supported Au catalysts, *Catal. Today* 111 (2006) 22–33.
- [6] S. Bordiga, E. Groppo, G. Agostini, J.A. van Bokhoven, C. Lamberti, Reactivity of surface species in heterogeneous catalysts probed by *in situ* X-ray absorption techniques, *Chem. Rev.* 113 (2013) 1736–1850.
- [7] E. Gross, J.M. Krier, L. Heinke, G.A. Somorjai, Building bridges in catalysis science. Monodispersed metallic nanoparticles for homogeneous catalysis and atomic scale characterization of catalysts under reaction conditions, *Top. Catal.* 55 (2012) 13–23.
- [8] C. Lamberti, A. Zecchina, E. Groppo, S. Bordiga, Probing the surfaces of heterogeneous catalysts by *in situ* IR spectroscopy, *Chem. Soc. Rev.* 39 (2010) 4951–5001.
- [9] B.M. Weckhuysen, Chemical imaging of spatial heterogeneities in catalytic solids at different length and time scales, *Angew. Chem. Int. Edit.* 48 (2009) 4910–4943.
- [10] F. Zaera, Probing liquid/solid interfaces at the molecular level, *Chem. Rev.* 112 (2012) 2920–2986.
- [11] B.M. Weckhuysen, Snapshots of a working catalyst: possibilities and limitations of *in situ* spectroscopy in the field of heterogeneous catalysis, *Chem. Commun.* (2002) 97–110.
- [12] C.W. Jones, F. Tao, M.V. Garland, Introduction to special issue on Operando and *in situ* studies of catalysis, *ACS Catal.* 2 (2012) 2444–2445.
- [13] M.S. Chen, D.W. Goodman, Catalytically active gold: from nanoparticles to ultrathin films, *Accounts Chem. Res.* 39 (2006) 739–746.
- [14] H.J. Freund, Model studies in heterogeneous catalysis, *Chem.-Eur. J.* 16 (2010) 9384–9397.
- [15] U. Landman, B. Yoon, C. Zhang, U. Heiz, M. Arenz, Factors in gold nanocatalysis: oxidation of CO in the non-scalable size regime, *Top. Catal.* 44 (2007) 145–158.
- [16] M.S. Chen, D.W. Goodman, The structure of catalytically active gold on titania, *Science* 306 (2004) 252–255.
- [17] M. Valden, X. Lai, D.W. Goodman, Onset of catalytic activity of gold clusters on titania with the appearance of nonmetallic properties, *Science* 281 (1998) 1647–1650.
- [18] B. Yoon, H. Hakkinen, U. Landman, A.S. Worz, J.M. Antonietti, S. Abbet, K. Judai, U. Heiz, Charging effects on bonding and catalyzed oxidation of CO on Au-8 clusters on MgO, *Science* 307 (2005) 403–407.
- [19] A. Boffa, C. Lin, A.T. Bell, G.A. Somorjai, Promotion of Co and Co₂ hydrogenation over Rh by metal-oxides – the influence of oxide Lewis acidity and reducibility, *J. Catal.* 149 (1994) 149–158.
- [20] A.B. Boffa, C. Lin, A.T. Bell, G.A. Somorjai, Lewis acidity as an explanation for oxide promotion of metals – implications of its importance and limits for catalytic reactions, *Catal. Lett.* 27 (1994) 243–249.
- [21] I.X. Green, W.J. Tang, M. Neurock, J.T. Yates, Spectroscopic observation of dual catalytic sites during oxidation of CO on a Au/TiO₂ catalyst, *Science* 333 (2011) 736–739.

- [22] E. Gross, M. Asscher, M. Lundwall, D.W. Goodman, Gold nanoclusters deposited on SiO₂ via water as buffer layer: CO-IRAS and TPD characterization, *J. Phys. Chem. C* 111 (2007) 16197–16201.
- [23] M.C. Kung, R.J. Davis, H.H. Kung, Understanding Au-catalyzed low-temperature CO oxidation, *J. Phys. Chem. C* 111 (2007) 11767–11775.
- [24] H.J. Freund, Metal-supported ultrathin oxide film systems as designable catalysts and catalytic supports, *Surf. Sci.* 601 (2007) 1438–1442.
- [25] C. Burda, X.B. Chen, R. Narayanan, M.A. El-Sayed, Chemistry and properties of nanocrystals of different shapes, *Chem. Rev.* 105 (2005) 1025–1102.
- [26] C.K. Tsung, J.N. Kuhn, W.Y. Huang, C. Aliaga, L.I. Hung, G.A. Somorjai, P.D. Yang, Sub-10 nm platinum nanocrystals with size and shape control: catalytic study for ethylene and pyrrole hydrogenation, *J. Am. Chem. Soc.* 131 (2009) 5816–5822.
- [27] S. Carrettin, P. Concepcion, A. Corma, J.M.L. Nieto, V.F. Puntes, Nanocrystalline CeO₂ increases the activity of an for CO oxidation by two orders of magnitude, *Angew. Chem. Int. Edit.* 43 (2004) 2538–2540.
- [28] P. Sonstrom, M. Baumer, Supported colloidal nanoparticles in heterogeneous gas phase catalysis: on the way to tailored catalysts, *Phys. Chem. Chem. Phys.* 13 (2011) 19270–19284.
- [29] C. Aliaga, J.Y. Park, Y. Yamada, H.S. Lee, C.K. Tsung, P.D. Yang, G.A. Somorjai, Sum frequency generation and catalytic reaction studies of the removal of organic capping agents from Pt nanoparticles by UV-ozone treatment, *J. Phys. Chem. C* 113 (2009) 6150–6155.
- [30] J.M. Krier, W.D. Michalak, L.R. Baker, K. An, K. Komvopoulos, G.A. Somorjai, Sum frequency generation vibrational spectroscopy of colloidal platinum nanoparticle catalysts: disordering versus removal of organic capping, *J. Phys. Chem. C* 116 (2012) 17540–17546.
- [31] J.A. Lopez-Sanchez, N. Dimitratos, C. Hammond, G.L. Brett, L. Kesavan, S. White, P. Miedziak, R. Tiruvalam, R.L. Jenkins, A.F. Carley, D. Knight, C.J. Kiely, G.J. Hutchings, Facile removal of stabilizer-ligands from supported gold nanoparticles, *Nat. Chem.* 3 (2011) 551–556.
- [32] L.R. Baker, G. Kennedy, M. Van Spronsen, A. Hervier, X.J. Cai, S.Y. Chen, L.W. Wang, G.A. Somorjai, Furfuraldehyde hydrogenation on titanium oxide-supported platinum nanoparticles studied by sum frequency generation vibrational spectroscopy: acid-base catalysis explains the molecular origin of strong metal-support interactions, *J. Am. Chem. Soc.* 134 (2012) 14208–14216.
- [33] F. Tao, S. Dag, L.W. Wang, Z. Liu, D.R. Butcher, H. Bluhm, M. Salmeron, G.A. Somorjai, Break-up of stepped platinum catalyst surfaces by high CO coverage, *Science* 327 (2010) 850–853.
- [34] F. Tao, M.E. Grass, Y.W. Zhang, D.R. Butcher, J.R. Renzas, Z. Liu, J.Y. Chung, B.S. Mun, M. Salmeron, G.A. Somorjai, Reaction-driven restructuring of Rh–Pd and Pt–Pd core-shell nanoparticles, *Science* 322 (2008) 932–934.
- [35] M.A. Newton, W. van Beek, Combining synchrotron-based X-ray techniques with vibrational spectroscopies for the in situ study of heterogeneous catalysts: a view from a bridge, *Chem. Soc. Rev.* 39 (2010) 4845–4863.
- [36] E. Stavitski, B.M. Weckhuysen, Infrared and Raman imaging of heterogeneous catalysts, *Chem. Soc. Rev.* 39 (2010) 4615–4625.
- [37] G. Kennedy, L.R. Baker, G.A. Somorjai, Selective amplification of C=O Bond Hydrogenation on Pt/TiO₂: catalytic reaction and sum-frequency generation vibrational spectroscopy studies of crotonaldehyde hydrogenation, *Angew. Chem. Int. Edit.* 53 (2014) 3405–3408.
- [38] F. Gao, Y.L. Wang, D.W. Goodman, Reaction kinetics and polarization-modulation infrared reflection absorption spectroscopy (PM-IRAS) investigation of CO oxidation over supported Pd–Au alloy catalysts, *J. Phys. Chem. C* 114 (2010) 4036–4043.
- [39] C. Rameshan, C. Weilach, W. Stadlmayr, S. Penner, H. Lorenz, M. Havecker, R. Blume, T. Rocha, D. Teschner, A. Knop-Gericke, R. Schlögl, D. Zemlyanov, N. Memmel, G. Rupprechter, B. Klotzer, Steam reforming of methanol on PdZn near-surface alloys on Pd(111) and Pd foil studied by in-situ XPS, LEIS and PM-IRAS, *J. Catal.* 276 (2010) 101–113.
- [40] X.Z. Shu, M. Zhang, Y. He, H. Frei, F.D. Toste, Dual visible light photoredox and gold-catalyzed arylation ring expansion, *J. Am. Chem. Soc.* 136 (2014) 5844–5847.
- [41] M. Zhang, M. de Respinis, H. Frei, Time-resolved observations of water oxidation intermediates on a cobalt oxide nanoparticle catalyst, *Nat. Chem.* 6 (2014) 362–367.
- [42] E. Gross, X.Z. Shu, S. Alayoglu, H.A. Bechtel, M.C. Martin, F.D. Toste, G.A. Somorjai, In situ IR and X-ray high spatial-resolution microspectroscopy measurements of multistep organic transformation in flow microreactor catalyzed by Au nanoclusters, *J. Am. Chem. Soc.* 136 (2014) 3624–3629.
- [43] E. Stavitski, M.H.F. Kox, I. Swart, F.M.F. de Groot, B.M. Weckhuysen, In situ synchrotron-based IR microspectroscopy to study catalytic reactions in zeolite crystals, *Angew. Chem. Int. Edit.* 47 (2008) 3543–3547.
- [44] A. Urakawa, N. Maeda, A. Baiker, Space- and time-resolved combined DRIFT and Raman spectroscopy: monitoring dynamic surface and bulk processes during NO(x) storage reduction, *Angew. Chem. Int. Edit.* 47 (2008) 9256–9259.
- [45] A.M. Beale, B.M. Weckhuysen, EXAFS as a tool to interrogate the size and shape of mono and bimetallic catalyst nanoparticles, *Phys. Chem. Chem. Phys.* 12 (2010) 5562–5574.
- [46] A.I. Frenkel, J.A. Rodriguez, J.G.G. Chen, Synchrotron techniques for in situ catalytic studies: capabilities, challenges, and opportunities, *ACS Catal.* 2 (2012) 2269–2280.
- [47] M. Ebner, F. Marone, M. Stampanoni, V. Wood, Visualization and quantification of electrochemical and mechanical degradation in Li ion batteries, *Science* 342 (2013) 716–720.
- [48] E.K. Gibson, M.W. Zandbergen, S.D.M. Jacques, C. Biao, R.J. Cernik, M.G. O'Brien, M. Di Michiel, B.M. Weckhuysen, A.M. Beale, Noninvasive spatiotemporal profiling of the processes of impregnation and drying within Mo/Al₂O₃ catalyst bodies by a combination of X-ray absorption tomography and diagonal offset Raman spectroscopy, *ACS Catal.* 3 (2013) 339–347.
- [49] J. Ruiz-Martinez, A.M. Beale, U. Deka, M.G. O'Brien, P.D. Quinn, J.F.W. Mosselmans, B.M. Weckhuysen, Correlating metal poisoning with zeolite deactivation in an individual catalyst particle by chemical and phase-sensitive X-ray microscopy, *Angew. Chem. Int. Edit.* 52 (2013) 5983–5987.
- [50] I.D. Gonzalez-Jimenez, K. Cats, T. Davidian, M. Ruitenbeek, F. Meirer, Y.J. Liu, J. Nelson, J.C. Andrews, P. Pianetta, F.M.F. de Groot, B.M. Weckhuysen, Hard X-ray nanotomography of catalytic solids at work, *Angew. Chem. Int. Edit.* 51 (2012) 11986–11990.
- [51] W.D. Michalak, J.M. Krier, K. Komvopoulos, G.A. Somorjai, Structure sensitivity in Pt nanoparticle catalysts for hydrogenation of 1,3-butadiene: in situ study of reaction intermediates using SFG vibrational spectroscopy, *J. Phys. Chem. C* 117 (2013) 1809–1817.
- [52] K. An, S. Alayoglu, N. Musselwhite, S. Plamthottam, G. Melaei, A.E. Lindeman, G.A. Somorjai, Enhanced CO oxidation rates at the interface of mesoporous oxides and Pt nanoparticles, *J. Am. Chem. Soc.* 135 (2013) 16689–16696.
- [53] G. Melaei, A.E. Lindeman, G.A. Somorjai, Cobalt particle size effects in the Fischer-Tropsch synthesis and in the hydrogenation of CO₂ studied with nanoparticle model catalysts on silica, *Top. Catal.* 57 (2014) 500–507.
- [54] V.V. Pushkarev, K.J. An, S. Alayoglu, S.K. Beaumont, G.A. Somorjai, Hydrogenation of benzene and toluene over size controlled Pt/SBA-15 catalysts: elucidation of the Pt particle size effect on reaction kinetics, *J. Catal.* 292 (2012) 64–72.
- [55] J.K. Norskov, T. Bligaard, B. Hvolbaek, F. Abild-Pedersen, I. Chorkendorff, C.H. Christensen, The nature of the active site in heterogeneous metal catalysis, *Chem Soc Rev* 37 (2008) 2163–2171.
- [56] L. Li, A.H. Larsen, N.A. Romero, V.A. Morozov, C. Glinsvad, F. Abild-Pedersen, J. Greeley, K.W. Jacobsen, J.K. Norskov, Investigation of catalytic finite-size-effects of platinum metal clusters, *J. Phys. Chem. Lett.* 4 (2013) 222–226.
- [57] C.J. Kiewer, C. Aliaga, M. Bieri, W.Y. Huang, C.K. Tsung, J.B. Wood, K. Komvopoulos, G.A. Somorjai, Furan hydrogenation over Pt(111) and Pt(100) single-crystal surfaces and Pt nanoparticles from 1 to 7 nm: a kinetic and sum frequency generation vibrational spectroscopy study, *J. Am. Chem. Soc.* 132 (2010) 13088–13095.
- [58] C.A. Witham, W.Y. Huang, C.K. Tsung, J.N. Kuhn, G.A. Somorjai, F.D. Toste, Converting homogeneous to heterogeneous in electrophilic catalysis using monodisperse metal nanoparticles, *Nat. Chem.* 2 (2010) 36–41.
- [59] C.H. Yoon, M.X. Yang, G.A. Somorjai, Hydrogenation of 1,3-butadiene on platinum surfaces of different structures, *Catal. Lett.* 46 (1997) 37–41.
- [60] E. Gross, G.A. Somorjai, The impact of electronic charge on catalytic reactivity and selectivity of metal-oxide supported metallic nanoparticles, *Top. Catal.* 56 (2013) 1049–1058.
- [61] A. Taguchi, F. Schuth, Ordered mesoporous materials in catalysis, *Micropor. Mesopor. Mat.* 77 (2005) 1–45.
- [62] D. Astruc, F. Lu, J.R. Aranzas, Nanoparticles as recyclable catalysts: the frontier between homogeneous and heterogeneous catalysis, *Angew. Chem. Int. Edit.* 44 (2005) 7852–7872.
- [63] E. Gross, J.H. Liu, S. Alayoglu, M.A. Marcus, S.C. Fakra, F.D. Toste, G.A. Somorjai, Asymmetric catalysis at the mesoscale: gold nanoclusters embedded in chiral self-assembled monolayer as heterogeneous catalyst for asymmetric reactions, *J. Am. Chem. Soc.* 135 (2013) 3881–3886.
- [64] E. Gross, J.H.C. Liu, F.D. Toste, G.A. Somorjai, Control of selectivity in heterogeneous catalysis by tuning nanoparticle properties and reactor residence time, *Nat. Chem.* 4 (2012) 947–952.
- [65] W.Y. Huang, J.H.C. Liu, P. Alayoglu, Y.M. Li, C.A. Witham, C.K. Tsung, F.D. Toste, G.A. Somorjai, Highly active heterogeneous palladium nanoparticle catalysts for homogeneous electrophilic reactions in solution and the utilization of a continuous flow reactor, *J. Am. Chem. Soc.* 132 (2010) 16771–16773.
- [66] Y.M. Li, J.H.C. Liu, C.A. Witham, W.Y. Huang, M.A. Marcus, S.C. Fakra, P. Alayoglu, Z.W. Zhu, C.M. Thompson, A. Arjun, K. Lee, E. Gross, F.D. Toste, G.A. Somorjai, A Pt-cluster-based heterogeneous catalyst for homogeneous catalytic reactions: X-ray absorption spectroscopy and reaction kinetic studies of their activity and stability against leaching, *J. Am. Chem. Soc.* 133 (2011) 13527–13533.
- [67] W. Huang, J.N. Kuhn, C.K. Tsung, Y. Zhang, S.E. Habas, P. Yang, G.A. Somorjai, Dendrimer templated synthesis of one nanometer Rh and Pt particles supported on mesoporous silica: catalytic activity for ethylene and pyrrole hydrogenation, *Nano Lett.* 8 (2008) 2027–2034.
- [68] A. Iglesias-Juez, A.M. Beale, K. Maaijen, T.C. Weng, P. Glatzel, B.M. Weckhuysen, A combined in situ time-resolved UV-Vis, Raman and high-energy resolution X-ray absorption spectroscopy study on the deactivation behavior of Pt and Pt–Sn propane dehydrogenation catalysts under industrial reaction conditions, *J. Catal.* 276 (2010) 268–279.
- [69] A. Patlolla, P. Baumann, W. Xu, S.D. Senanayake, J.A. Rodriguez, A.I. Frenkel, Characterization of metal-oxide catalysts in operando conditions by combining X-ray absorption and Raman spectroscopies in the same experiment, *Top. Catal.* 56 (2013) 896–904.
- [70] A.M. Beale, M.G. O'Brien, M. Kasunic, A. Golobic, M. Sanchez-Sanchez, A.J.W. Lobo, D.W. Lewis, D.S. Wragg, S. Nikitenko, W. Bras, B.M. Weckhuysen, Probing ZnAPO-34 self-assembly using simultaneous multiple in situ techniques, *J. Phys. Chem. C* 115 (2011) 6331–6340.

- [71] F.M.F. de Groot, E. de Smit, M.M. van Schooneveld, L.R. Aramburo, B.M. Weckhuysen, In-situ scanning transmission X-ray microscopy of catalytic solids and related nanomaterials, *ChemPhysChem* 11 (2010) 951–962.
- [72] J.R. Jinschek, Advances in the environmental transmission electron microscope (ETEM) for nanoscale in situ studies of gas-solid interactions, *Chem. Commun.* 50 (2014) 2696–2706.
- [73] I.L.C. Buurmans, B.M. Weckhuysen, Heterogeneities of individual catalyst particles in space and time as monitored by spectroscopy, *Nat. Chem.* 4 (2012) 873–886.
- [74] K.H. Cats, I.D. Gonzalez-Jimenez, Y.J. Liu, J. Nelson, D. van Campen, F. Meirer, A.M.J. van der Eerden, F.M.F. de Groot, J.C. Andrews, B.M. Weckhuysen, X-ray nanoscopy of cobalt Fischer-Tropsch catalysts at work, *Chem. Commun.* 49 (2013) 4622–4624.
- [75] H.A. Bechtel, E.A. Muller, R.L. Olmon, M.C. Martin, M.B. Raschke, Ultrabroadband infrared nanospectroscopic imaging, *Proc. Natl. Acad. Sci. USA* 111 (2014) 7191–7196.
- [76] J. Stadler, T. Schmid, R. Zenobi, Nanoscale chemical imaging using top-illumination tip-enhanced Raman spectroscopy, *Nano. Lett.* 10 (2010) 4514–4520.
- [77] E.M. van Schroyen Lantman, T. Deckert-Gaudig, A.J.G. Mank, V. Deckert, B.M. Weckhuysen, Catalytic processes monitored at the nanoscale with tip-enhanced Raman spectroscopy, *Nature Nano* 7 (2012) 583–586.